

Using a portable muon detector for radioactive source measurements and recognition

Joaquin Masias¹, Franco Delgado¹, Lucía Coll¹, Alicia Pérez¹, José Bazo¹, Alberto Gago¹

¹*Sección Física, Departamento de Ciencias, Pontificia Universidad Católica del Perú, Av. Universitaria 1801, Lima 32, Perú*

June 11, 2022

Abstract

We have re-purposed portable plastic scintillator muon detectors, designed by the CosmicWatch project, for the measurement of electrons emitted by the decay of radioactive sources. For the latter purpose we have first calibrated the detectors using the local atmospheric muon flux, performing angular distribution and attenuation measurements. In addition, we have simulated the detector using Geant4 in a detailed fashion for a cross-check and better understanding of the device. Then, we have developed a method to evaluate the activity of β -sources and to discriminate different sources by looking into their respective voltage spectrum output. Thus we are able to distinguish between different β -sources.

1 Introduction

In order to detect charged particles, especially muons, several portable devices have been designed. These devices are based on different technologies such as plastic scintillators [1, 2], silicon pixels [3] and drift tubes [4]. For this work, we have assembled and used hand-held scintillation-based detectors developed for the CosmicWatch project [5, 6].

This detector can measure muons that are produced in the upper layers of the atmosphere. Muon production occurs when cosmic rays, mainly protons, interact with nuclei in the atmosphere, producing secondary particles, which then decay into muons [7]. Muons are highly penetrating, a property that allows us to detect them under different conditions (e.g. inside buildings or below ground level).

In this paper, we will prove that this detector, after minor modifications, can be used to count electrons as well. By doing this, we will be able to measure radioactive β -sources activity and identify different elements using their measured spectrum. Other plastic scintillator detectors have also been used for β -sources measurements [8, 9, 10].

This paper is divided as follows: we first describe in Sec. 2 the detector. Then, in Sec. 3 we outline how we performed simulations of the detector under different configurations to cross-check the physics involved. In Sec. 4 we describe the calibration process using atmospheric muon measurements and simulations. Then in Sec. 5 we describe the method and give the results on the measurement of the radioactive β -sources activities and source recognition.

2 Desktop Muon Detector

The Desktop Muon Detector (DMD), a design of the CosmicWatch project from the Massachusetts Institute of Tech-

nology, is a scintillation based device [5]. The core of the detector is a plastic scintillator approximately 5 cm \times 5 cm \times 1 cm polystyrene Dow Styron 663 W doped with 1% PPO + 0.03% POPOP [11]. We have measured its optical properties, as shown in Fig. 1, corroborating that it is blue-emitting (peak emission at \approx 420 nm) and has an absorption cut-off at \approx 400 nm. When a charged particle passes through the plastic, it leaves a fraction of its energy and the medium emits scintillation light. A SensL C-Series SMT silicon photomultiplier (SiPM) [12] (6.0 \times 6.0 mm²), attached to the plastic, detects these scintillation photons. The SiPM is connected to the rest of the voltage processing circuit and the plastic scintillator block is wrapped in reflective foil and insulating tape.

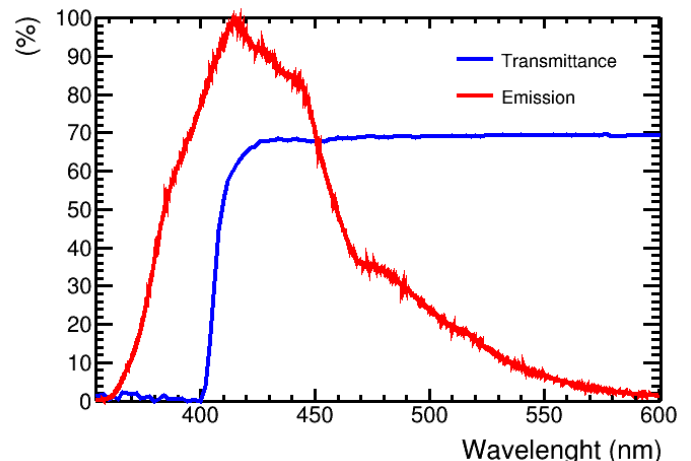


Figure 1: Measured transmittance (spectrophotometer) and emission (photoluminescence spectroscopy) for the polystyrene doped with 1% PPO + 0.03% POPOP scintillator.

The bare detector is mounted in a light-tight aluminum casing ($6.6 \times 7.4 \times 4.0 \text{ cm}^3$). The main printed circuit board (PCB) amplifies and shapes the SiPM signal that is then processed by a micro-controller, an Arduino Nano. Its configuration script [13] allows us to control the OLED screen and data acquisition conditions and display data in real time.

The detector is powered through a mini-USB to USB connector. An event is recorded, if the signal passed a given threshold of 35 ADC (analog-to-digital converter). A file with each event's recorded data, including its pulse amplitude, time and deadtime, can be written using a Python script.

3 Simulations with Geant4

In order to compare to measurements, we have developed simulations in Geant4 [14], a CERN toolkit that simulates the passage of particles through matter. The simulation scripts can be found in the supplementary material [15]. We simulate the geometry of the DMD (Fig. 2) as a plastic scintillator (i.e. BC408 plastic) with a complete description of its optical and electromagnetic properties (refraction index, absorption length, scintillation, wavelength shift properties, etc.), along with the silicon sensor inside the aluminum casing. The circuitry was not included in the simulation.

The criteria used to trigger an event count is that a particle inside the plastic scintillator generates optical photons that reach the SiPM's area. For every particle in the detector, we can collect information, including deposited energy and number of generated photons. Using the simulation, we calculate the geometrical efficiency of the configuration for photon collection at the SiPM. For atmospheric muons this efficiency is on average 76%. Moreover, we include the SiPM energy-dependent efficiency [12], which is 41% at its peak 424 nm. We also model simple barriers and large structures (e.g. a 4-storey building) to simulate cosmic ray attenuation.

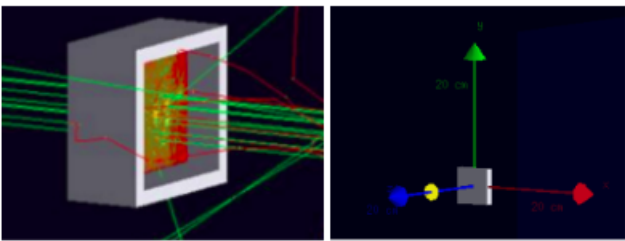


Figure 2: Geant4 DMD simulation geometry. Left: muon beam, Right: cylindrical radioactive source

In addition, we use the theoretical atmospheric muon flux, including its angle and energy dependence [16], as the injected particle distribution. Since the flux depends on the location, we use the flux at Lima, Peru's coordinates and altitude, where the measurements were performed. For the radioactive source activity calculations, we simulate a cylindrical source of height 0.3 cm and radius 1.1 cm, as shown in Fig. 2, at a given distance from the DMD and force its decay.

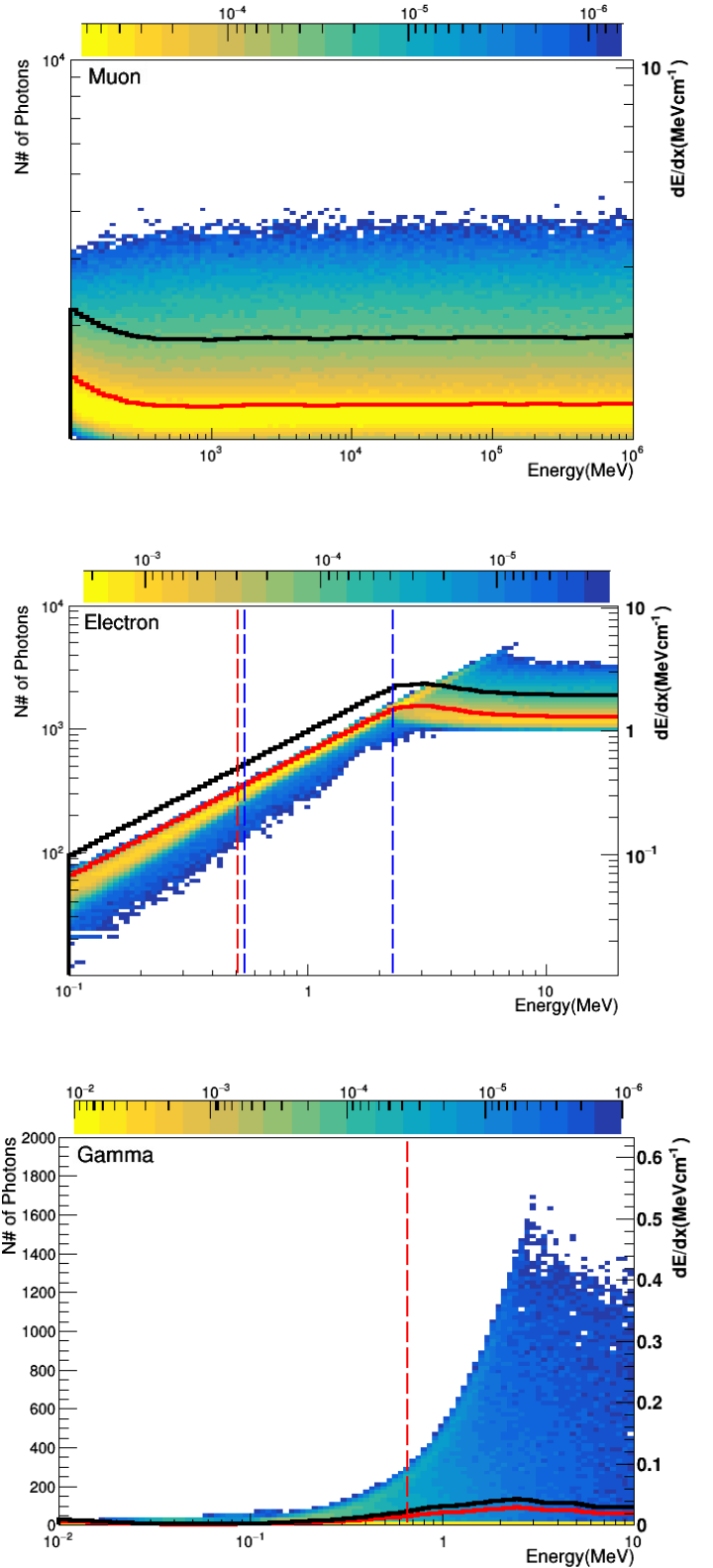


Figure 3: Normalized 2D distribution of the simulated number of photons produced in the scintillator versus the energy of vertically incident muons (top), electrons (middle), and gamma rays (bottom). The black line shows the deposited dE/dx in the scintillator, the red line the photon production reconstructed from Birks' law using the dE/dx and the dashed lines the maximum β and γ energies for ^{137}Cs in red, and for ^{90}Sr and ^{90}Y in blue.

In Fig. 3 we show the simulations' results for the optical photon production and dE/dx (shown in black) by muons, electrons and gamma rays as a function of their energy. Photon production in a scintillator can be described by Birk's law [17]:

$$\frac{dL}{dx} = S \frac{\frac{dE}{dx}}{1 + k_B \frac{dE}{dx}} \quad (1)$$

where L is the light yield, S represents the scintillation efficiency, k_B is Birk's constant and dE/dx the mean energy loss per path length of the particle. For large dE/dx the equation behaves nonlinearly.

In the case of muons, the mean energy loss can be obtained with the Bethe-Bloch formula [18]. If this energy loss is taken from the simulation and used in Eq. 1, the resulting photon production as a function of energy, shown with a red line in Fig. 3, can explain the simulation results. Muons show Minimum Ionizing Particle (MIP) behavior very early in their energy spectrum, with 1300 photons produced on average.

Electrons, on the other hand, deposit most of their energy and have a linear photon production up to ~ 3 MeV, meaning that electrons of two different energies can be distinguished from their number of generated photons. This behaviour will be later useful for differentiating radioactive sources. In fact, we are highlighting in Fig. 3 the energies of the two radioactive sources that we will later use, which are producing distinguishable amounts of photons. At energies higher than 3 MeV, electrons start showing MIP-like behavior, where their average photon production is also around 1300 photons.

Low-energy gamma rays produce almost no optical photons in the scintillator, as seen in Fig. 3. For energies greater than 0.1 MeV the main photon production mechanism is Compton scattering. As shown, there is a relatively low probability of emitting hundreds of photons, thus the average number of produced optical photons (red line) is hardly increased.

4 Detector Calibration with atmospheric muons

DMDs are rather novel technology, and even though their structure is simple, their behaviour has been not fully characterized. Due to slight differences in the circuitry and SiPM to plastic coupling, a DMD may have a higher sensitivity or higher background noise, producing differences in the measured event rate. Therefore, an absolute calibration is needed.

Detectors have similar time dependence for the same kind of measurement (Fig. 4), for a short period of time, where no major atmospheric, seasonal or solar effects are relevant. Thus we prove the stability of the detectors. The average deadtime per registered event is 15 ms.

The total expected muon flux is $1.16 \text{ cm}^{-2}\text{min}^{-1}$, based on an average rate calculated with PARMA/EXPACS [19], using a 60 m altitude and different parameters according

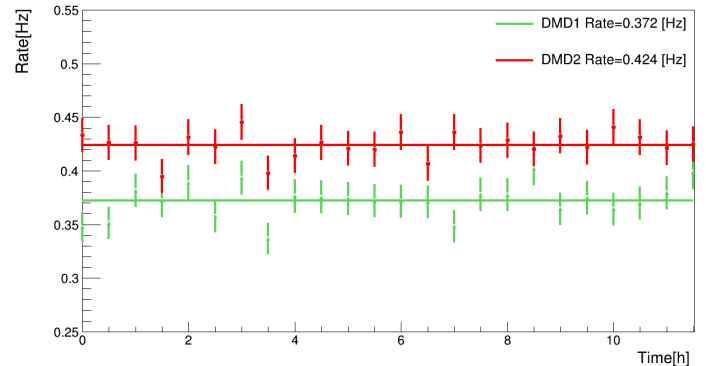


Figure 4: Rate (averaged every 30 minutes) for single detectors at 60 m.a.s.l. at $12^\circ S 77^\circ W$. The rate time dependence is similar for both detectors.

to the registered solar activity at various stages of the solar cycle. The expected total rate for a DMD is 0.484 s^{-1} , resulting in a measured 76.8% and 87.6% efficiency for the two used detectors. As described in Sec. 3, the geometrical efficiency of the detector for atmospheric muons is 76%. Additional events could be attributed to the circuit's background noise or a not complete light-tight enclosure.

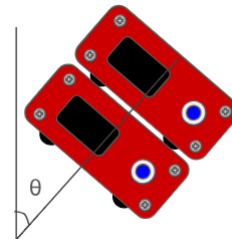


Figure 5: Setup for coincidence measurements of the atmospheric muon angular distribution.

4.1 Angular distribution

The first check of the detector's performance is done with the angular distribution of the atmospheric muon flux. We performed coincidence measurements, using two DMDs placed one on top of the other, as shown in Fig. 5, to reduce the aperture uncertainty.

We use an offline trigger with time gap of less than 0.01 s to count measurements in both DMDs as a single coincident event. These measurements were taken for ten hours, in an open space to avoid attenuation effects, at $0^\circ, 22.5^\circ, 45^\circ, 67.5^\circ,$ and 90° with respect to the zenith.

In Fig. 6 we show the comparison between measurements and simulation. The measured data are in agreement with the simulation within 0.4σ . Muon's energy loss and decay depend on the height of their production layer and amount of material traversed[20]. The muon flux, then, decreases as the zenith angle increases, since at larger angles there is a higher chance of interaction in the atmosphere due to the longer distances muons must travel to reach the detector.

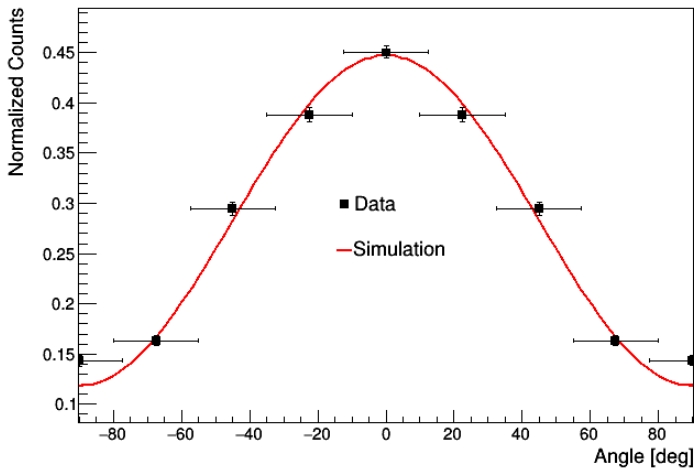


Figure 6: Normalized angular distribution of atmospheric muons, obtained using coincident events with two DMDs (black squares). The red curve is the simulation which follows a $\cos^2(\theta)$ distribution ($\chi_{red}^2 = 8.4$). Data are mirrored around 0° .

The measured distribution fits well ($\chi_{red}^2 = 8.4$) with a $\cos^2(\theta)$, which is expected from the theoretical distribution.

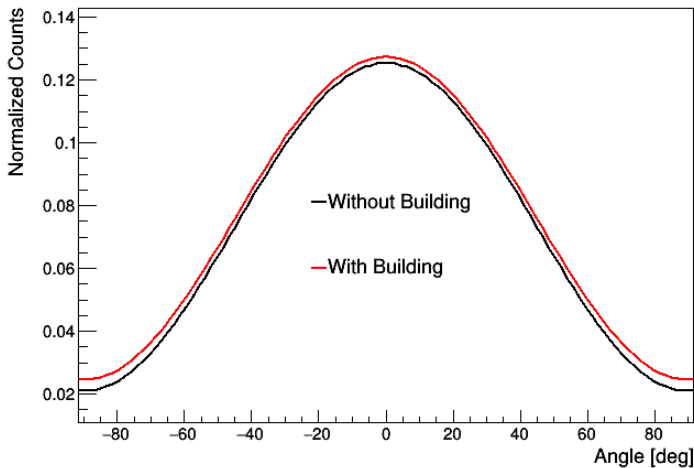


Figure 7: Atmospheric muon angular distribution simulation comparing building attenuation. Normalized with the number of total events. Data are mirrored around 0° .

4.2 Attenuation

Next we look for attenuation effects due to large structures on the atmospheric muon flux. We simulate the Physics Department building, where we made our measurements. The toy simulation is a four story building, with an area of 4 m^2 , built of concrete. We considered an average density of 1.5 g/cm^3 and do not include windows, beams, nor columns.

As seen in Fig. 7, the simulated angular distributions without and including the building are alike, suggesting that the atmospheric muons are not deflected and do not interact with the building. However, we were actually also measuring secondary electrons produced from the muon in-

teractions with concrete, as shown next.

As a further analysis, we study the effect of muon attenuation in four settings: the detector on an open field, with a single 1.5 cm lead plate, alone inside the previously described building, and with the lead barrier inside the building. First, we considered a comparison between the detector on an open field and shielded with the lead plate. For the simulation, muons are directed towards a $10 \times 10 \text{ m}^2$ area (much larger than the detector) and a million events are generated. The measurements were two hours each. The ratio, Table 1, is almost one in both cases (simulation and measurement). There is no difference between the measured rate at an open field and below an 1.5 cm thick lead plate.

We then considered the detector without the lead plate inside the four storey building and on an open field. The results, Table 1, were once again very close to one. We can then conclude that separately, both the lead plate and the building, produce no visible attenuation.

	lead openfield	building openfield
Measurement	0.99 ± 0.01	0.99 ± 0.01
Simulation	1.01 ± 0.01	1.01 ± 0.06

Table 1: Ratio of events with the detector in different configurations

Finally, we considered a combined measurement (lead plate and building). Looking in the MC truth at the particles that reach the detector (Table 2), we see that there are more events without muons (i.e. only caused by electrons) in the combined attenuated simulation, but there are less total events. Then, we conclude that the building attenuates the cosmic-ray flux creating secondary particles (electrons) that produce photons in the scintillator that are detected by the SiPM. The ratio of measurements decreases considerably when in addition to the building a shielding lead plate is used. Data (0.87 ± 0.02) and simulation (0.93 ± 0.06) are in agreement within 1σ . Thus, we conclude that secondary electrons are produced inside the building, and that these are stopped by the lead plate.

	Open field	Building	Lead	Combined
Events	525 ± 23	528 ± 23	531 ± 23	490 ± 22
No μ^-	52 ± 7	65 ± 8	67 ± 8	74 ± 8
e^-/event	0.3 ± 0.03	0.5 ± 0.04	0.3 ± 0.03	0.4 ± 0.03

Table 2: Simulation of charged particles in the detector. Combined refers to simultaneous use of the building and lead plate. Events without muons (No μ^-) are events with only electrons. The simulation is based on one million generated events.

5 Source Activity and Recognition

Even if the original design of the DMD was made for muon identification, we are going to prove next that it can also be used to measure charged particles, as electrons. For this

purpose we make measurements on radioactive beta sources using the DMD.

It is important to note that for measuring electrons it is required to remove the DMD's aluminum shielding. For isolating the radioactive source signal we need to subtract the atmospheric muon background. Then, we perform simultaneous measurements with two DMDs. From now on, we will call them DMD1 and DMD2. DMD1 is directly exposed to the β source, giving R_{S+B} , the signal plus background rate. DMD2 is kept as control, measuring the muon background rate, R_B . The simultaneity of the measurements is due to possible time variations in the muon atmospheric background, producing two different backgrounds if we made the measurements at different times with a single detector. In order to make comparable the measurements of the muon background rates of these two different detectors, we make simultaneous measurements of the aforementioned rates obtaining a relative efficiency factor that we will call η , defined in Eq. 2. This factor allows us to convert the rates between the two detectors. We can then obtain the pure signal rate, R_S (see Eq. 3), by subtracting the atmospheric muon background counted with the control DMD2.

$$\eta = \frac{R_B^{\text{DMD1}}}{R_B^{\text{DMD2}}} \quad (2)$$

$$R_S^{\text{DMD1}} = R_{S+B}^{\text{DMD1}} - \eta \times R_B^{\text{DMD2}} \quad (3)$$

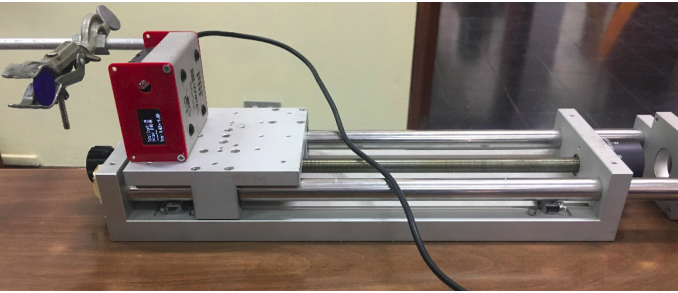


Figure 8: Setup for radioactive source measurements at fixed distances. The DMD has the half of its aluminum case facing the source removed. The DMD is placed on top of the precision platform, while the radioactive source disk is held fixed.

To maintain a standard distance between source and DMD we used a precision platform. This setup is shown in Fig. 8. We did an experimental cross-check to verify that the source intensity diminishes with the square of the distance as seen in Fig. 9. This point approximation holds up to 5 cm.

5.1 Activity measurement

We used two radioactive isotopes for this study: ^{90}Sr and ^{137}Cs . Both decay through pure β emission. ^{90}Sr ($t_{1/2} = 28.79$ yr) emits an electron ($E_{max} = 0.546$ MeV) going to ^{90}Y , which is also a β emitter ($E_{max} = 2.28$ MeV, $t_{1/2} = 64$ hours). ^{137}Cs ($t_{1/2} = 30.17$ yr) emits an electron ($E_{max} = 0.514$ MeV) going to ^{137m}Ba , which is a γ emitter ($E = 0.66$ MeV, $t_{1/2} = 153$ s). As a result, ^{137}Cs has effectively a large γ component.

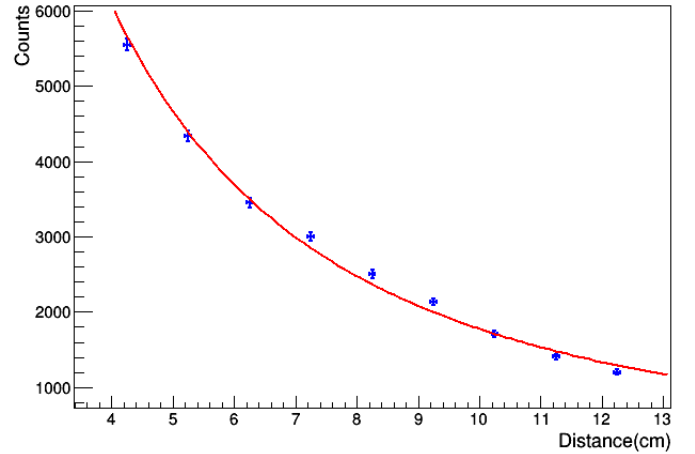


Figure 9: Inverse squared law of a ^{90}Sr source measured using a DMD ($\chi^2_{red} = 4.1$).

We measured the background subtracted rates (see Eq. 3) of two sources of ^{90}Sr and two sources of ^{137}Cs , each with a different activity as shown in Table 3. From this point onward, rate refers to the background subtracted rate. The lower activity sources are referred to as A, while the higher ones as B. We made two hour measurements at 5 cm for ^{90}Sr sources and at 0.5 cm for ^{137}Cs . The closer distance for ^{137}Cs is due to its lower rate, which at the larger distance was compatible with the muon background.

The activities at the time of observation are calculated from their initial activities and their production year. ^{137}Cs rates are lower than ^{90}Sr , in spite of their respective activities being higher. This is because ^{90}Sr , through the ^{90}Y decay, produces more energetic electrons, which emit more scintillation photons (see Fig. 3). On the other hand, gammas from ^{137m}Ba , product of ^{137}Cs , are practically invisible to the DMDs, as simulated in Fig. 3. This has been corroborated by testing the DMD's response to a ^{55}Fe source ($t_{1/2} = 2.74$ yr, activity $1 \mu\text{Ci}$) which is an X-ray (5-6 keV) and Auger electron (5.19 keV) emitter. At these energies there is neither photon, nor electron detection.

The activities can be extrapolated from the DMDs measured rates (Table 3) and then compared with the *actual* ones. In order to estimate the activity we obtain first a conversion factor ($\alpha = \text{Activity}_A / \text{Rate}_A$), which depends on the isotope, the detector and the distance. Then the activity for other sources of the same isotope can be calculated using this conversion factor and the measured rate with the same detector and distance ($\text{Activity}_B = \alpha \text{Rate}_B$). The extrapolated activity of source B obtained with the conversion factor from source A are in both cases (^{90}Sr and ^{137}Cs) within 1σ of the known activity, as shown in Table 3. In the case of ^{137}Cs , the estimation has an additional uncertainty that arises from the specific geometry of the sources, which cannot be considered a point source at the given distance.

5.2 Source recognition

We have developed Geant4 simulations showing that β -sources recognition is possible using a plastic scintillator. A

Source	Rate(Hz)	Activity(μCi)	
		(expected)	(extrapolated)
^{137}Cs A	1.01 ± 0.01	0.23 ± 0.01	
^{137}Cs B	6.53 ± 0.03	1.77 ± 0.40^a	1.49 ± 0.07
^{90}Sr A	6.16 ± 0.03	0.065 ± 0.002	
^{90}Sr B	9.16 ± 0.04	0.093 ± 0.002	0.097 ± 0.003

Table 3: Beta sources background subtracted rates measured for two hours, expected and extrapolated activities. The ^{90}Sr (^{137}Cs) measurements were done at a distance of 5 cm (0.5 cm) from the detector. The expected activities are calculated from their initial factory activities and production year and their uncertainties are taken as one year, since only the purchase year is known.

^aThis activity was obtained using a GAMMA-SCOUTTM since the source's production year was unknown. The error on the measurement is included.

difference in the produced optical photon spectra between atmospheric muons and radioactive beta sources must reflect on their respective measured voltage spectra, as seen in Fig. 10. In this way, we can identify radioactive β -sources.

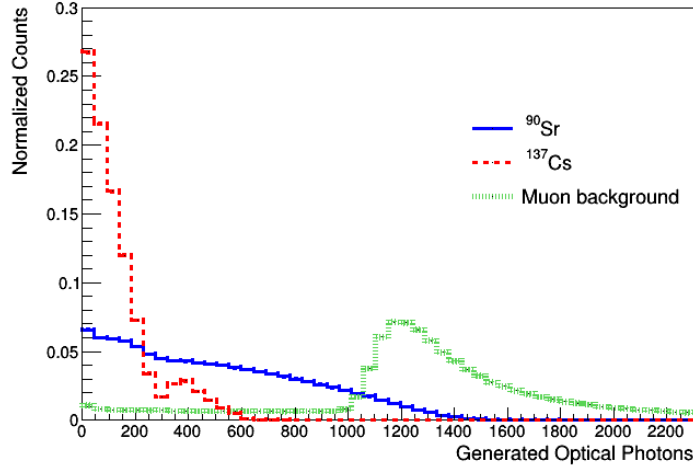


Figure 10: Normalized optical photon production comparison for simulated beta sources and muon background.

We then analyze the voltage spectrum for each source, shown in Fig. 11. Because of slight differences in the assembly process, the voltage spectrum is different for each detector, so the same DMD must be used for every measurement. A 25 mV threshold is applied in order to remove the noise from the DMD. Because of this, the peak from ^{137}Cs corresponding to the least energetic events seen in Fig. 10 is discarded.

We used Kolmogorov–Smirnov tests to prove that their voltage spectra were distinguishable from the atmospheric muon background and from those of different radioactive isotopes. To compare two sources the significance level α is calculated, as presented in Fig. 12. For ^{90}Sr we conclude that the source is different from background within 3σ , while with 76% C.L. it is different from ^{137}Cs . In the case of ^{137}Cs , its spectrum is with 70% C.L. different than that from the atmospheric muon background.

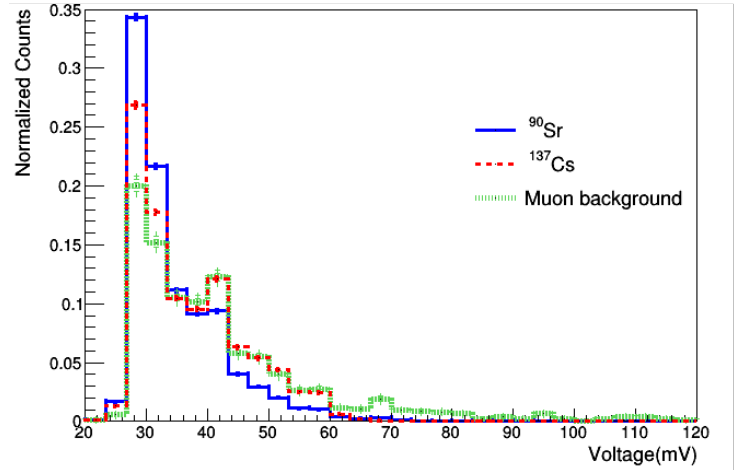


Figure 11: Normalized measured SiPM voltage spectra for the atmospheric muon background and background-subtracted radioactive sources with the highest activity. Events with voltages > 70 correspond almost exclusively to the muon background.

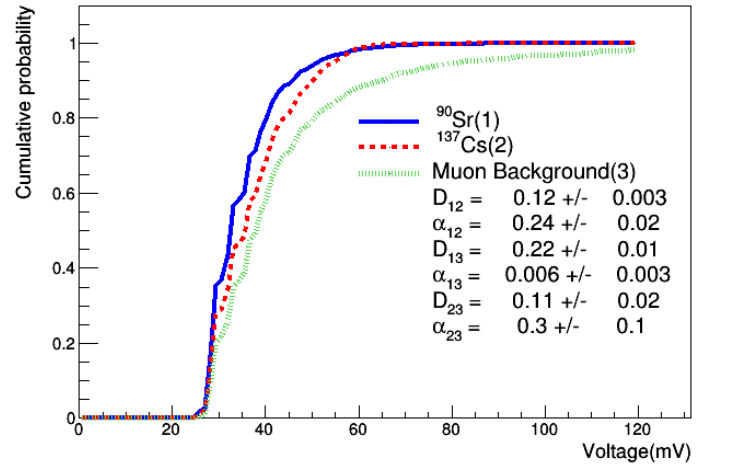


Figure 12: Kolmogorov–Smirnov tests comparing radioactive sources and muon background. The D parameter represents the maximum distance between distributions and α is the significance level. The sample size (i.e. number or bins) is 100.

The sources of the same isotope were found to be indistinguishable, to a confidence level better than 90%, between different samples of the same isotope (^{90}Sr : $\alpha=0.994 \pm 0.003$, ^{137}Cs : $\alpha=0.913 \pm 0.024$).

6 Conclusions

We have used a new design of a portable muon detector based on a plastic scintillator with a SiPM light detector. We have calibrated and evaluated the performance of the detector by measuring and simulating the local atmospheric muon angular flux. As expected, its angular distribution follows a $\cos^2(\theta)$ function. We have also measured the attenuation to the muon flux inside a building and showed that secondary electrons are produced due to the passing

of muons.

We have extended the use of the muon detector to measurements of radioactive β -sources. Using simultaneously two detectors we can obtain the background-subtracted signal rate from the sources. For the proof of concept we used two β -emitting sources: ^{90}Sr and ^{137}Cs , each with two disks of different activities. Our analysis was divided in two parts: finding a factor to convert measured rates into activities for each source and contrasting, through Kolmogorov–Smirnov tests, the voltage spectra of the sources to tell if they are similar or different. We found that these detectors can in fact be used to determine the source’s current activity and to identify the specific isotope using a recognition method. Experimentally, we found that a distance of at least 5 cm must be kept between the detector and the source (to avoid systematical uncertainties), and that the sources rate at that distance must be at least equal to that of the atmospheric muon background in order to do a proper analysis.

7 Acknowledgements

This work was funded by the Dirección de Gestión de la Investigación at PUCP under grant No. DGI-2017-3-0019 (CAP) and DGI-2018-5-0010 (PAIN). The authors would like to thank J. Conrad, S. Axani and C. Argüelles, for useful discussions, suggestions and reading of the manuscript, as well as for the detector components donations that made this work possible. We would also wish to thank the Nuclear Tracks Group for letting us use their radioactive sources and equipment, R. Sánchez and J. A. Guerra for the measurements of the plastic scintillator’s optical properties.

References

- [1] B. Baumbaugh, J. Bishop, L. Castle, D. Karmgard, J. Kozminski, J. Marchant, P. Mooney, R. Ruchti, and D. Wiand, “A portable cosmic ray detector and display,” in *Nuclear Science Symposium and Medical Imaging Conference*, vol. 2, pp. 783–785, 1999.
- [2] E. Aguayo, R. Kouzes, and J. L. Orrell, “Development of a Portable Muon Witness System,” tech. rep., Pacific Northwest National Lab. (PNNL), 2011.
- [3] V. Greco, “A desk cosmic ray detector for schools using the ALPIDE chip,” *ALICE Matters*, 2017.
- [4] W. Chavez, K. Harriger, N. Kallas, and W. Maier, “Portable Muon Tracker,” tech. rep., New Mexico Tech, 2013.
- [5] S. N. Axani, J. M. Conrad, and C. Kirby, “The Desktop Muon Detector: A simple, physics-motivated machine- and electronics-shop project for university students,” *Am. J. Phys.*, vol. 85, p. 948, 2017.
- [6] S. N. Axani, K. Frankiewicz, and J. M. Conrad, “The CosmicWatch Desktop Muon Detector: a self-contained, pocket sized particle detector,” *JINST*, vol. 13, no. 03, p. P03019, 2018.
- [7] T. K. Gaisser, *Cosmic Rays and Particle Physics*, pp. 40–41. Cambridge University Press, 1991.
- [8] D. Krona, “Development of a portable β - spectrometer for in situ measurements of Sr-90 and Y-90 using a plastic scintillator and a silicon photomultiplier (SiPM),” Master’s thesis, Medical Radiation Physics, Lund University, 2015.
- [9] J. S. Nam, Y. S. Choi, S. B. Hong, B. K. Seo, J. K. Moon, and J. W. Choi, “Study on the Characteristics of a Scintillator for Beta-ray Detection using Epoxy Resin,” in *ICRS-13 & RPSD-2016*, vol. 153, EPJ Web of Conferences, 2017.
- [10] I. M. M. A. Medeiros, C. B. Zamboni, J. A. G. de Medeiros, V. X. de Oliveira, M. F. Koskinas, S. P. Camargo, and L. D. Junior, “Applicability study of plastic scintillation detectors for beta radiation measurements,” tech. rep., IPEN-CNEN/SP, 1997.
- [11] A. Pla-Dalmau, A. Bross, V. Rykalin, and B. Wood, “Extruded plastic scintillator for MINERvA,” in *IEEE Nuclear Science Symposium Conference Record*, IEEE, 2005.
- [12] “SensL C-Series SiPM datasheet.” <http://sensl.com/downloads/ds/DS-MicroCseries.pdf>. Accessed: 2018-10-20.
- [13] S. Axani, “CosmicWatch-Desktop-Muon-Detector.” GitHub repository <https://github.com/spenceraxani/CosmicWatch-Desktop-Muon-Detector>, 2018.
- [14] S. Agostinelli *et al.*, “GEANT4: A Simulation toolkit,” *Nucl. Instrum. Meth.*, vol. A506, pp. 250–303, 2003.
- [15] J. Masias, “Geant4 simulation of Desktop Muon Detector.” GitHub repository <https://github.com/Jmasias04/Geant4-Simulation-of-Desktop-Muon-Detector>, 2019.
- [16] P. Shukla and S. Sankrith, “Energy and angular distributions of atmospheric muons at the Earth,” *Int. J. Mod. Phys.*, vol. A33, no. 30, p. 1850175, 2018.
- [17] J. B. Birks, *The Theory and Practice of Scintillation Counting*, pp. 187–188. Manchester: Pergamon Press, second ed., 1967.
- [18] P. Sigmund, *Particle Penetration and Radiation Effects*, pp. 163–169. Germany: Springer, first ed., 2006.
- [19] T. Sato, “Analytical Model for Estimating Terrestrial Cosmic Ray Fluxes Nearly Anytime and Anywhere in the World: Extension of PARMA/EXPACS,” *PLOS ONE*, vol. 10, no. 12, pp. 1–33, 2015.
- [20] I. Braun, J. Engler, J. Horandel, and J. Milke, “Forbush decreases and solar events seen in the 10-20 GeV energy range by the Karlsruhe Muon Telescope,” *Advances in Space Research*, vol. 43, pp. 480–488, 10 2008.